



Dual-active sites design of $\text{Sn}_x\text{-Sb}_y\text{-O-GO}$ nanosheets for enhancing electrochemical CO_2 reduction via Sb-accelerating water activation

Haichuan He^a, Jian Wu^a, Xiao Yu^a, Dan Xia^a, Yan Wang^a, Fei Chen^a, Liqiang Wang^b, Linlin Wu^a, Jianhan Huang^a, Ning Zhao^c, Liu Deng^{a,*}, You-Nian Liu^{a,*}

^a Hunan Provincial Key Laboratory of Micro & Nano Materials Interface Science, College of Chemistry and Chemical Engineering, Central South University, Changsha, Hunan 410083, PR China

^b Henan Province Industrial Technology Research Institute of Resources and Materials, School of Material Science and Engineering, Zhengzhou University, Zhengzhou, Henan 450001, PR China

^c State Key Laboratory of Coal Conversion, Institute of Coal Chemistry, Chinese Academy of Sciences, Taiyuan, Shanxi 030001, PR China



ARTICLE INFO

Keywords:

Dual-active site

Carbon dioxide reduction

Sn/Sb -based electrocatalyst

Formic acid

ABSTRACT

Electrochemical CO_2 reduction reaction (e CO_2 RR) is a promising approach for the sustainable development of energy and environment, yet the control over selectivity of e CO_2 RR is challenging and entails intelligent active site design. Herein, we firstly propose dual-active sites design of $\text{Sn}_x\text{-Sb}_y\text{-O-GO}$ nanosheets (NSs) for controlling the reaction pathways. The $\text{Sn}_x\text{-Sb}_y\text{-O-GO}$ NSs catalyst possesses large-size ultrathin structure and controllable Sn/Sb ratio, strengthening the interaction at the active site with OCHO^* intermediate. The optimized $\text{Sn}_7\text{-Sb}_3\text{-O-GO}$ NSs exhibit a HCOOH selectivity of 96.5% and partial current density of $\sim 21.6 \text{ mA cm}^{-2}$. The experiments and theory calculations show that the introduction of Sb secondary active site can accelerate water activation for forming unique ${}^* \text{H}$ species and the binding strength of OCHO^* key intermediates, thereby enhancing the HCOOH selectivity in e CO_2 RR. This work lends credence to the novel metal-metal dual-active sites design strategy for e CO_2 RR sustainable energy conversion.

1. Introduction

Electrochemical CO_2 reduction reaction (e CO_2 RR) to value-added chemicals or fuels offers a sustainable approach to solve the problems of energy and environment, owing to its easy operation, electrochemical valorization, and scalability [1–5]. However, the control over selectivity of e CO_2 RR is still challenging, due to the inert C=O bond (806 kJ mol^{-2}) in CO_2 molecule, the competitive hydrogen evolution reaction (HER) in aqueous solution, as well as up to 16 diverse liquid or gas products from the extremely complicated reaction pathways of e CO_2 RR [6–10]. Thus, it is imperative to develop electrocatalysts with novel active sites for facilitating the kinetic behavior, tailoring the key intermediates, and controlling reaction pathways, thereby achieving highly efficient e CO_2 RR with targeted products.

Recently, dual-active sites (DAS) strategy has been proved to be a powerful method to tailor the activity of e CO_2 RR catalysts [11–15], because the introduction of the secondary site can lead to the orbital interactions, or activate the subsidiary molecule (like H_2O) for forming unique species (${}^* \text{H}$), which result in the adaptable adsorption behavior

of key intermediates and controlling reaction pathways [16–18]. For example, Liao and co-workers cooperated CuO₄ site (CO-producing site) and CuPc site (C₂H₄-producing site) to realize the desirable ${}^* \text{CO}$ generation and ${}^* \text{CO}$ intermediate dimerization, respectively, thereby promoting performance for the electrocatalytic reduction of CO_2 to C₂H₄ [19]. Wang et al. reported that sulfur in sulfur doped oxide-derived indium was acted as the active site for generating hydrogen species (${}^* \text{H}$), which enhances the e CO_2 RR to HCOOH on indium catalysts [20]. Theoretical and experimental studies on the engineering dual-active sites have mainly focused on non-metallic element, like S and N, attempting to manipulate the interaction between two metal active sites have rarely reported yet [21,22]. The metal element which located at the left-hand branch of Trassati's volcano curve, including Ag, Sn and In, typically possess weak metal-hydrogen bond and low HER activity, which contribute to appropriate selectivity and activity for enhanced e CO_2 RR performance [23,24]. Therefore, metal-metal DAS have attracted particular interest due to significant e CO_2 RR selectivity with highly desirable products.

Sn-based materials are one of the most promising catalysts for the

* Corresponding authors.

E-mail addresses: dengliu@csu.edu.cn (L. Deng), liuyounian@csu.edu.cn (Y.-N. Liu).

practical eCO₂RR systems, as their activation capacity of CO₂ and environmentally friendly features [25–32]. Nevertheless, their selectivity for carbon products of eCO₂RR is limited by the competitive CO and HCOOH pathway (see Table S2 in the supporting information). Besides, the inevitable HER in aqueous solution seriously affects the activity and selectivity of eCO₂RR [33–35]. Catalysts based on Sn with In, Cu, Ag or Pd, have been fabricated to optimize selectivity for CO or HCOOH [36–41]. The selectivity alternation generally ascribed to the control of the surface electronic state and biding energy of the Sn active sites via the combination of foreign metal atoms. However, the role of secondary metal active site in reaction pathways control and intermediates modulation are ambiguous in catalysts. Moreover, the exposure of active sites, as well as prohibiting detachment and agglomeration, is also key factors in the catalytic process and catalyst durability [42–44]. Therefore, it is desirable to develop an exposed and uniform Sn based dual-active sites for selectivity eCO₂RR catalysts, as well as clarify their principle of selectivity and promotion effect.

Herein, we firstly construct a series of large-size ultrathin dual-active sites Sn_x-Sb_y-O-GO NSs electrocatalysts for controllably tuning eCO₂RR to HCOOH (Scheme 1). The optimized Sn₇-Sb₃-O-GO NSs exhibit an excellent HCOOH Faradaic efficiency (FE) of 96.5% and a HCOOH partial current density (j_{HCOOH}) of -21.6 mA cm^{-2} at the potential of -1.1 V (vs. RHE) in 0.5 M KHCO₃ solution, as well as long durability over 21 h. Electrochemical performance test, *in situ* attenuated total reflectance-Fourier transform infrared (in situ ATR-FTIR) and density functional theory (DFT) calculations demonstrate that the elaborate Sn-Sb dual-active sites design fulfills three principles: (i) these Sn_x-Sb_y-O-GO NSs can heighten the kinetics, tailor the key intermediates, and control reaction pathways, due to their ultrahigh surface-to-volume ratio, controllable Sn/Sb ratio, and unique eCO₂RR catalytic property; (ii) the introduction of high electronegativity of Sb to SnO₂ promotes the electron flow from Sn to Sb, thus strengthening the interaction at the active site with the OCHO* intermediates; (iii) the Sb active site can assist water activation for forming unique *H species, and promoting the binding strength of OCHO* key intermediates on Sn_x-Sb_y-O-GO NSs surfaces, boosting the selectivity for HCOOH over CO.

2. Experimental Section

2.1. Chemicals and materials

Potassium persulfate (K₂S₂O₈), phosphorus(V) oxide (P₂O₅), sulfuric acid (H₂SO₄), potassium permanganate (KMnO₄), hydrogen peroxide (H₂O₂), hydrochloric acid (HCl), tin (IV) chloride pentahydrate (SnCl₄), antimony trichloride (SbCl₃), N-Ethyl-4-piperidinocarboxamide hydrochloride, ethylene glycol, ethanol, and potassium bicarbonate (KHCO₃) were purchased from Sinopharm (Shanghai, China). Graphite powder (particle size < 20 μm), nafion solution, and Nafion@ 117 film were obtained from Alfa Aesar. CO₂ (99.99%), N₂ (99.99%) were purchased from Saizhong Gas (Changsha, China).

2.2. Synthesis of 2D Graphene oxide nanosheets

Graphene oxide (GO) was fabricated by a typical process. Firstly, graphite powder was subjected to pre-oxidation: graphite powder (3 g), P₂O₅ (2.5 g), K₂S₂O₈ (2.5 g), and H₂SO₄ (15 mL) were mixed under stirring vigorously at 80 °C for 6 h. The pre-oxidized graphite powders were rinsed with H₂O and ethanol, and dried at 60 °C for 12 h. Subsequently, KMnO₄ (7.5 g) was slowly added into the mixture of pre-oxidized graphite powder (1.7 g) and H₂SO₄ (60 mL) with vigorous stirring in an ice bath. The mixture was then transferred to 35 °C water bath and stirring for 1 h. Pure water (125 mL) and H₂O₂ solution (360 mL, 8.5 wt%) were added respectively, then kept for 5 h at 35 °C. Afterwards, the warm solution was filtered and rinsed with 1 L of 2 M HCl, then with pure H₂O before freeze-drying.

2.3. Synthesis of large-size ultrathin 2D dual-active sites Sn_x-Sb_y-O-GO NSs

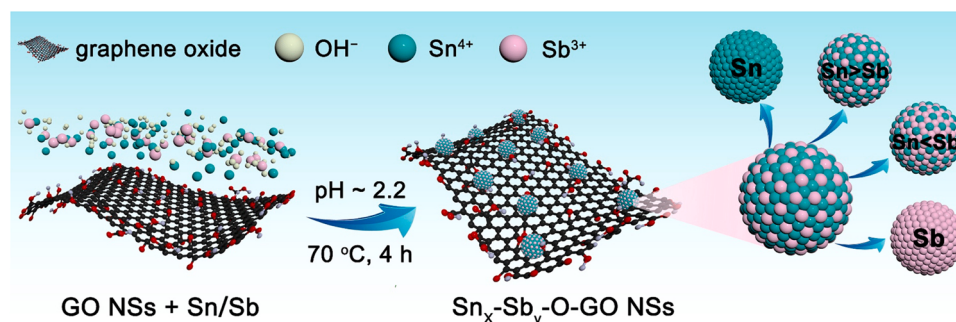
Firstly, a glycinesodium hydroxide buffer solution with pH 2.2 was prepared by dispersing glycine (2.07 g), H₂O (88 mL) and HCl (2.0 mL) in 462 mL ethylene glycol. Then, GO (15 mg), SnCl₄ (0.75-x mmol), and SbCl₃ (x mol) were added in 150 mL buffer solution and dispersed by ultrasound for 15 min. Subsequently, the mixture was incubated with vigorously stirring at 70 °C for 4 h. After washing and drying, the controllable Sn/Sb ratio large-size dual-active sites Sn_x-Sb_y-O-GO NSs were synthesized. The SnO₂-GO NSs and Sb₂O₅-GO NSs were synthesized by the same method.

3. Results and discussion

3.1. Synthesis and characterizations of the catalysts

A series of large-size ultrathin dual-active sites Sn_x-Sb_y-O-GO NSs were synthesized by a single-step process (Scheme 1). The different ratios of Sn and Sb metal ions and GO NSs are mixed in the buffer solution with strong agitation to obtain the different samples, where metal ions can be coordinated to –COOH or –OH functional groups on the surface of GO NSs and form Sn_x-Sb_y-O-GO NSs. The pristine SnO₂-GO and Sb₂O₅-GO NSs were also synthesized through similar procedure except for the addition of single Sn⁴⁺ or Sb³⁺. When the molar ratio of Sn (x) to Sb (y) are 9:1, 8:2, 7:3, 6:4, 5:5, 4:6, 3:7, 1:0 and 0:1, samples are marked as Sn₉-Sb₁-O-GO, Sn₈-Sb₂-O-GO, Sn₇-Sb₃-O-GO, Sn₆-Sb₄-O-GO, Sn₅-Sb₅-O-GO, Sn₄-Sb₆-O-GO, Sn₃-Sb₇-O-GO, SnO₂-GO and Sb₂O₅-GO NSs, respectively.

The high-resolution transmission electron microscopy (HR-TEM) images reveal that the morphology of all Sn_x-Sb_y-O-GO samples are large-size ultrathin NSs (Fig. 1 and Fig. S1). The size of the NSs can be tuned up to 5 μm. Particularly, compared with the single interplanar spacing of 0.334 nm in HR-TEM image of SnO₂-GO NSs (Fig. 1b), there appears the significant lattice deformation in the planes of cassiterite SnO₂ in Sn₇-Sb₃-O-GO NSs, which indicates that Sb was doped into the



Scheme 1. Schematic illustration of the preparation process of the large-size ultrathin dual-active sites Sn_x-Sb_y-O-GO NSs.

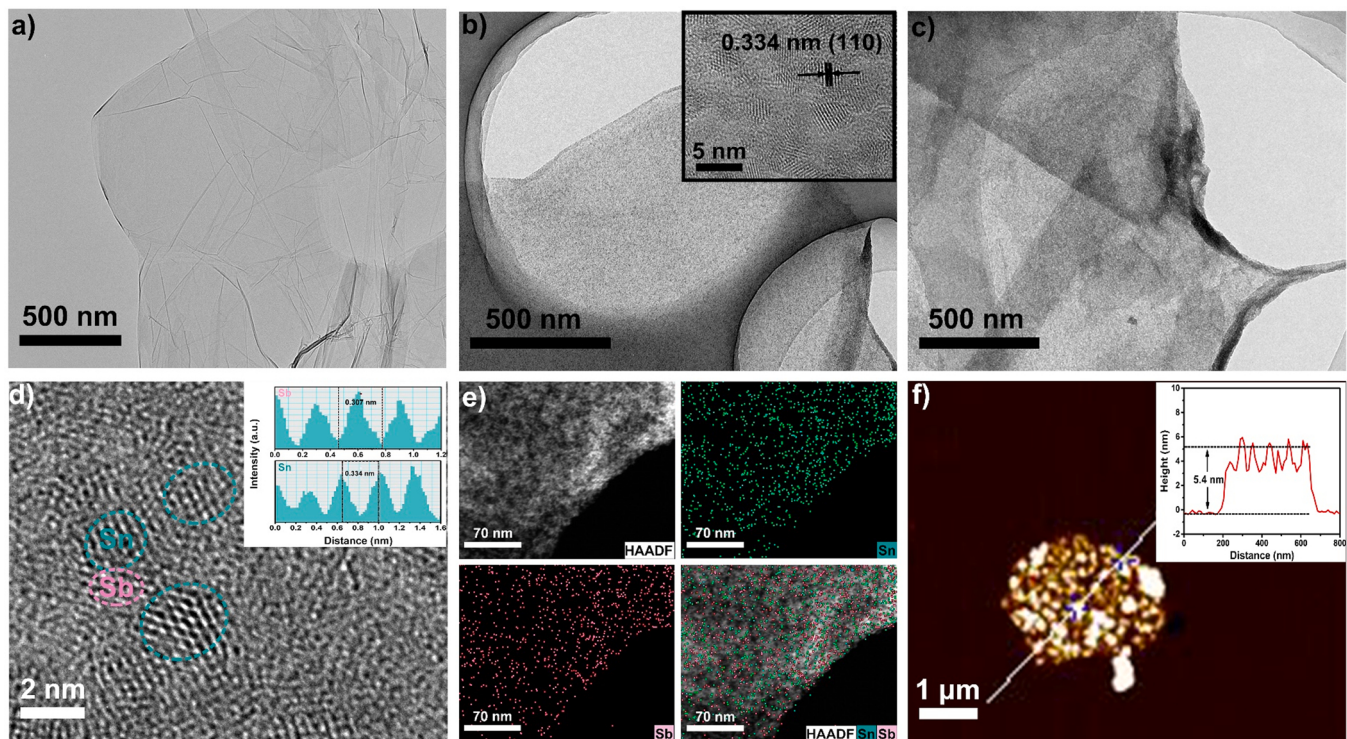


Fig. 1. Synthesis and structural characterization. TEM images of a) GO NSs, b) SnO_2 -GO NSs (the inset is high-resolution TEM image), c) $\text{Sn}_7\text{-O-Sb}_3$ -GO NSs. d) High-resolution TEM of $\text{Sn}_7\text{-O-Sb}_3$ -GO NSs (the inset is the images of lattice spacing intensity profiles). e) The corresponding elemental mappings and f) the atomic force microscopy image for $\text{Sn}_7\text{-O-Sb}_3$ -GO NSs.

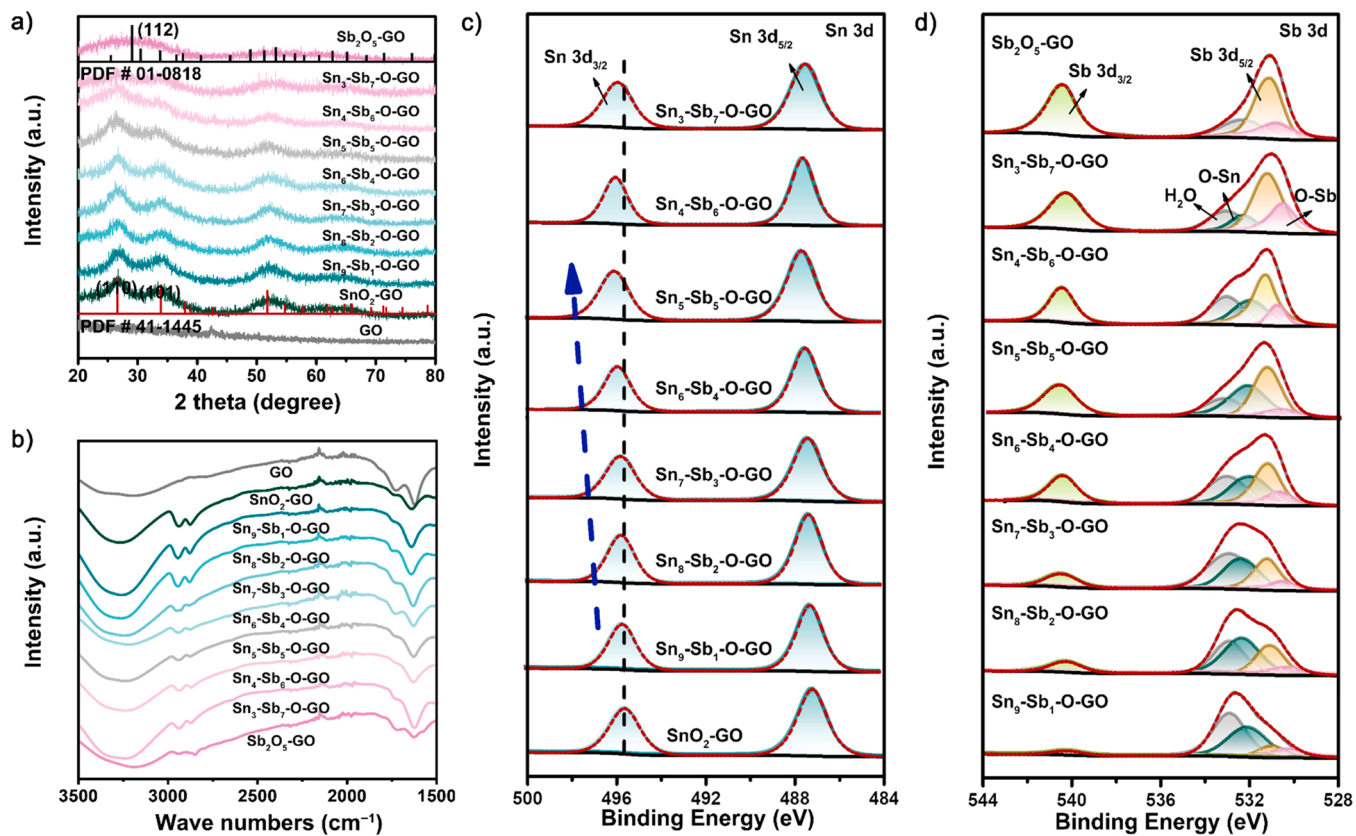


Fig. 2. a) XRD spectra, b) FTIR spectra, c) Sn 3d core level XPS spectra and d) Sb 3d core level XPS spectra of GO, SnO_2 -GO, $\text{Sn}_9\text{-Sb}_1\text{-O-GO}$, $\text{Sn}_8\text{-Sb}_2\text{-O-GO}$, $\text{Sn}_7\text{-Sb}_3\text{-O-GO}$, $\text{Sn}_6\text{-Sb}_4\text{-O-GO}$, $\text{Sn}_5\text{-Sb}_5\text{-O-GO}$, $\text{Sn}_4\text{-Sb}_6\text{-O-GO}$, $\text{Sn}_3\text{-Sb}_7\text{-O-GO}$ and Sb_2O_5 -GO NSs.

crystal lattice of SnO_2 (Fig. 1c & d) [45,46]. Meanwhile, small amounts of (112) planes of cervantite Sb_2O_5 appear, further proving that only few Sb_2O_5 species exist in $\text{Sn}_7\text{-Sb}_3\text{-O-GO}$ NSs. Moreover, the HR-TEM image of $\text{Sn}_8\text{-Sb}_2\text{-O-GO}$ only shows the lattice deformation of Sb-doped SnO_2 in Fig. S2. The high-angle annular darkfield scanning transmission electron microscopy (HAADF-STEM) analysis for $\text{Sn}_7\text{-Sb}_3\text{-O-GO}$ NSs also confirmed that both Sn and Sb elements existed and distributed uniformly over the NSs (Fig. 1e). The atomic force microscopy (AFM) is carried out to determine the thickness of $\text{Sn}_7\text{-Sb}_3\text{-O-GO}$ NSs. As shown in Fig. 1f, the thickness of ultrathin layered structure is about 3–5 nm, which is thin enough to present quantum confinement effects and ultrahigh surface-to-volume ratio, making for the exposure of active sites and prohibiting detachment and agglomeration.

Besides, to further investigate the crystalline structure and material compositions of the prepared $\text{Sn}_x\text{-Sb}_y\text{-O-GO}$ NSs, a series of characterization, the X-ray diffraction (XRD), Fourier transform infrared spectroscopy (FTIR) and inductively coupled plasma optical emission spectrometry (ICP-OES) were carried out. From Fig. 2a, the XRD patterns of the as-prepared $\text{SnO}_2\text{-GO}$ and $\text{Sb}_2\text{O}_5\text{-GO}$ NSs are consistent with the typical diffraction peaks of cassiterite SnO_2 (PDF # 41-1445) and cervantite Sb_2O_5 (PDF # 01-0818), respectively. The XRD patterns of $\text{Sn}_x\text{-Sb}_y\text{-O-GO}$ NSs with low Sb content exhibits similar diffraction peaks of the cassiterite $\text{SnO}_2\text{-GO}$ NSs. As the Sb content increased, extra diffraction peaks at 29.0° (112) assigned to cervantite Sb_2O_5 appeared, and the diffraction peaks at 26.6° (110) and 33.9° (101) peaks for cassiterite SnO_2 disappeared. Similarly, the composition of Sn and Sb in the $\text{Sn}_x\text{-Sb}_y\text{-O-GO}$ NSs were also measured by FTIR spectra. As shown in Fig. 2b, the peaks around 1600 cm^{-1} are attributed to the C=C stretching peak of GO NSs, and shift to lower frequencies owing to the enhanced interaction effect between the $\text{Sn}_x\text{-Sb}_y\text{-O}$ and GO NSs. There are two additive peaks at range of $2800 - 2900\text{ cm}^{-1}$, which indicate the existence of Sn-O or Sb-O, moreover, the peaks shift to lower wave numbers with the increase of Sb-O. The ICP-OES analysis further reveals the definite content of $\text{Sn}_x\text{-Sb}_y\text{-O-GO}$ NSs, the results are summarized in Table S1, which are numerically similar with the controlling ratio of Sn/Sb in reaction system.

The interaction between Sn-Sb dual-active sites was further analyzed by X-ray photoelectron spectroscopy (XPS). The C 1 s spectra for all $\text{Sn}_x\text{-Sb}_y\text{-O-GO}$ NSs show three peaks at 284.8, 286.7 and 288.6 eV, representing the C-C, C-O and C=O bonds (Fig. S3), respectively [47]. In the Sn 3d XPS spectra of the prepared samples, the peaks at 495.9 and 487.5 eV are attributed to Sn 3d_{3/2} and 3d_{5/2} (Fig. 2c), respectively, which confirm the oxidation state of Sn^{4+} . Because of the similar binding energy, the O 1 s and Sb 3d_{5/2} peaks are partly overlapping. The overlapping peaks can break up into four peaks representing the O 1 s peaks for H-O, O-Sn and O-Sb bonds at 533.2, 532.2 and 530.6 eV, respectively. Meanwhile, the characteristic peaks of spin-orbit-split Sb 3d_{3/2} and Sn 3d_{5/2} are located at 540.4 and 531.3 eV, respectively, confirming the oxidation state of Sb^{5+} as shown in Fig. 2d. The binding energies of Sb 3d_{3/2} are gradually increased with the increase of Sb content, indicating the controllable synthesis of $\text{Sn}_x\text{-Sb}_y\text{-O-GO}$ NSs (Fig. S4). Compared with $\text{SnO}_2\text{-GO}$ and $\text{Sb}_2\text{O}_5\text{-GO}$ NSs, all $\text{Sn}_x\text{-Sb}_y\text{-O-GO}$ NSs show simultaneously the characteristic peak of the O-Sn and O-Sb bonds, where the ratio of O-Sn to O-Sb is consistent with the trend of the Sn/Sb ratio (Fig. S5). Most importantly, in comparison to $\text{SnO}_2\text{-GO}$ NSs, the two peaks of Sn 3d shift to higher binding energy with the incorporation of Sb, as well as a shift trend to lower binding energy is also found in characteristic peak of Sb 3d_{5/2}, suggesting an electron transfer from Sn to doped Sb due to the higher electronegativity of Sb than Sn.

3.2. Electrocatalytic CO_2 reduction performance of catalysts

The e CO_2 RR performances of these large-size ultrathin $\text{Sn}_x\text{-Sb}_y\text{-O-GO}$, $\text{SnO}_2\text{-GO}$, $\text{Sb}_2\text{O}_5\text{-GO}$ and GO NSs were explored in the CO_2 -saturated 0.5 M KHCO_3 electrolyte with Nafion-membrane separated

airtight H-type cell (See Supporting Information for detailed methods). All the potentials reported in this work were converted into values versus reversible hydrogen electrode (vs. RHE). The linear sweep voltammetry (LSV) curves show that all $\text{Sn}_x\text{-Sb}_y\text{-O-GO}$ and pristine $\text{SnO}_2\text{-GO}$ NSs exhibit effective e CO_2 RR catalytic activity (Fig. S6), where the current density shows dependence behaviour on Sb content (Fig. S7). The current density in CO_2 -saturated and N_2 -saturated KHCO_3 electrolyte for $\text{Sb}_2\text{O}_5\text{-GO}$ and GO NSs is almost unanimous. To further evaluate the e CO_2 RR activity and selectivity, the products are collected and analysed by gas chromatography (GC) and ^1H NMR. The main product of $\text{Sb}_2\text{O}_5\text{-GO}$ and GO NSs is H_2 , confirming the cathodic current densities mainly from HER and little activity from e CO_2 RR (Fig. S8). The main product of both $\text{SnO}_2\text{-GO}$ and $\text{Sn}_x\text{-Sb}_y\text{-O-GO}$ NSs were HCOOH (Fig. 3a). The optimized $\text{Sn}_7\text{-Sb}_3\text{-O-GO}$ NSs deliver a high HCOOH Faradaic efficiency (FE) over 80% in a wide and moderate potential range from -0.6 to -1.3 V and a highest FE of 96.5% at -1.1 V with a total current density of -22.4 mA cm^{-2} (Fig. 3b), which are superior to $\text{SnO}_2\text{-GO}$ NSs of 73.0% and other $\text{Sn}_x\text{-Sb}_y\text{-O-GO}$ NSs ($\text{Sn}_9\text{-Sb}_1\text{-O-GO}$ NSs of 82.1%, $\text{Sn}_8\text{-Sb}_2\text{-O-GO}$ NSs of 90.2%, $\text{Sn}_6\text{-Sb}_4\text{-O-GO}$ NSs of 92.1%, $\text{Sn}_5\text{-Sb}_5\text{-O-GO}$ NSs of 87.5%, $\text{Sn}_4\text{-Sb}_6\text{-O-GO}$ NSs of 78.7%, $\text{Sn}_3\text{-Sb}_7\text{-O-GO}$ NSs of 49.9%). Especially $\text{Sn}_7\text{-Sb}_3\text{-O-GO}$ NSs catalyst exhibits better e CO_2 RR performance among the reported results for Sn-based catalysts (listed in Table S2). Besides, $\text{Sn}_8\text{-Sb}_2\text{-O-GO}$ NSs catalyst also shows better HCOOH selectivity than that of $\text{SnO}_2\text{-GO}$ NSs, which suggests that the main active site in $\text{Sn}_x\text{-Sb}_y\text{-O-GO}$ catalysts is Sb-doped SnO_2 . In addition, as shown in Fig. 3c, a long-time electrolysis under potential of -1.1 V was carried out, and no declines in the HCOOH FE and current density are observed over 21 h, indicating excellent stability of $\text{Sn}_3\text{-Sb}_7\text{-O-GO}$ for e CO_2 RR. The above results demonstrate that the present $\text{Sn}_3\text{-Sb}_7\text{-O-GO}$ catalyst exhibits superior selectivity at high current density and thus high reaction rate, which is very promising for e CO_2 RR to HCOOH.

To understand the role of Sb deeply, the e CO_2 RR performance of the serials of $\text{Sn}_x\text{-Sb}_y\text{-O-GO}$ NSs catalysts are studied in detail. The e CO_2 RR activity of HCOOH increase significantly with an increase in Sb content up to 26.6 at% ($\text{Sn}_7\text{-Sb}_3\text{-O-GO}$) (Fig. 3d), whereas the formation rates of H_2 and CO are significantly inhibited at the same time (Fig. 3e & f). However, a further increase in Sb content leads to the decrease in the formation rate of HCOOH (Fig. 3g). To exclude the HER contribution in CO_2 -saturated KHCO_3 electrolyte, the partial current densities on the catalysts are measured (Fig. S9). From Fig. 3h and Fig. S10, it can be clearly found that the HCOOH and H_2 partial current densities are increased with the Sb content, whereas that of CO is lower in $\text{Sn}_x\text{-Sb}_y\text{-O-GO}$ than $\text{SnO}_2\text{-GO}$. These phenomena suggest that HCOOH generation through the incorporation of Sb into the SnO_2 , significantly increases at the expense of CO generation, rather than the hydrogen evolution. Unlike conventional doped e CO_2 RR catalyst, this result suggests that the dissociation of water is involved in the determining step for e CO_2 RR to HCOOH on $\text{Sn}_x\text{-Sb}_y\text{-O-GO}$ catalysts, since H^* is a requisite substrate for the reduction of CO_2 to HCOOH. In our system, in N_2 -saturated KHCO_3 electrolyte, the formation rate of H_2 is also found to increase with an increase in Sb content in the $\text{Sn}_x\text{-Sb}_y\text{-O-GO}$ catalysts. Recent studies reported that the role of Sb in promotion of the dissociation of H_2O via the formation of Sb-OH intermedium [48]. To further study the role of H_2O activation in the e CO_2 RR of our catalysts, the effect of electrolyte pH on e CO_2 RR for $\text{SnO}_2\text{-GO}$ and $\text{Sn}_7\text{-Sb}_3\text{-O-GO}$ NSs were be carried out. In the pH value following sequence of $\text{K}_2\text{HPO}_4 < \text{KHCO}_3 < \text{K}_2\text{SO}_4$, the ratio of formation rates of HCOOH for $\text{Sn}_7\text{-Sb}_3\text{-O-GO}$ NSs and $\text{SnO}_2\text{-GO}$ NSs are increasing from 1.31 in K_2HPO_4 to 1.82 in KHCO_3 and further to 2.01 in K_2SO_4 (Fig. S11), which indicate that the introduction of Sb assist the H_2O activation and form unique ${}^*\text{H}$ species to better enhance the formation of HCOOH in a higher pH value [20,49]. It is proposed that the introduction of Sb secondary active site into SnO_2 can facilitate the production of HCOOH via accelerating the activation of H_2O , as well as inhibiting CO_2 to CO process.

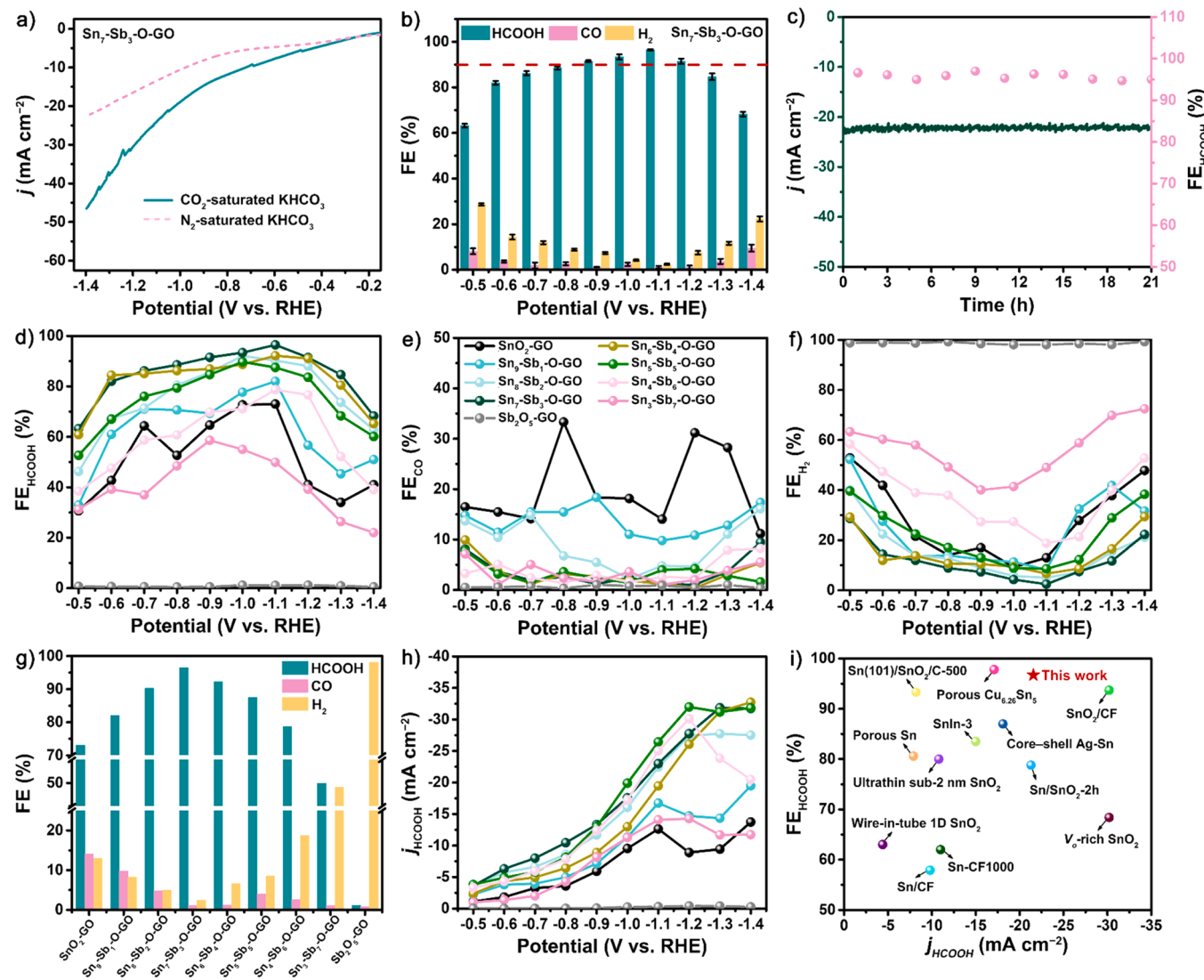


Fig. 3. a) LSV curves of $\text{Sn}_7\text{-Sb}_3\text{-O-GO}$ NSs in N_2 -saturated and CO_2 -saturated 0.5 M KHCO_3 . b) FE and c) stability test at -1.1 V for $\text{Sn}_7\text{-Sb}_3\text{-O-GO}$ NSs. d) HCOOH FE, e) CO FE, f) H_2 FE, g) the FE at -1.1 V and h) HCOOH partial current density for $\text{SnO}_2\text{-GO}$, $\text{Sn}_9\text{-Sb}_1\text{-O-GO}$, $\text{Sn}_8\text{-Sb}_2\text{-O-GO}$, $\text{Sn}_7\text{-Sb}_3\text{-O-GO}$, $\text{Sn}_6\text{-Sb}_4\text{-O-GO}$, $\text{Sn}_5\text{-Sb}_5\text{-O-GO}$, $\text{Sn}_4\text{-Sb}_6\text{-O-GO}$, $\text{Sn}_3\text{-Sb}_7\text{-O-GO}$ NSs, and $\text{Sb}_2\text{O}_5\text{-GO}$. i) FE and current density of CO_2 to HCOOH of the catalysts reported in the literature.

3.3. Experimental and theoretical study of the catalytic mechanism of $\text{Sn}_x\text{-Sb}_y\text{-O-GO}$

To clarify the reaction pathways of the $\text{Sn}_7\text{-Sb}_3\text{-O-GO}$ NSs, *in situ* ATR-FTIR measurement was carried out. The different spectrums for $\text{Sn}_7\text{-Sb}_3\text{-O-GO}$ and $\text{SnO}_2\text{-GO}$ NSs at the applied potentials varied from -0.5 to -1.4 V are shown in Fig. 4a & b. The two characteristic bands centred at 1542 and 1647 cm^{-1} ascribed to the characteristic peaks of $^{*}\text{CO}_2^-$ intermediates suggests that $\text{Sn}_7\text{-Sb}_3\text{-O-GO}$ and $\text{SnO}_2\text{-GO}$ NSs all have good eCO₂RR activity [35,50]. The peaks centered around 1393 and 1453 cm^{-1} are assigned to OCHO^* species. The peak centered around 1231 cm^{-1} can be the OH deformation of $^{*}\text{COOH}$. Different from $\text{SnO}_2\text{-GO}$ NSs, the $^{*}\text{COOH}$ characteristic band of $\text{Sn}_7\text{-Sb}_3\text{-O-GO}$ NSs is obviously suppressed at 1231 cm^{-1} . Meanwhile, two catalysts show no typical peaks $^{*}\text{CO}$ located at 1900 – 2100 cm^{-1} , suggesting no C_{2+} products pathways. The spectroscopic results demonstrate that the incorporation of Sb secondary active site into SnO_2 can inhibit CO_2 to CO process and promote to form oxygen coordinated OCHO^* key intermediates on $\text{Sn}_7\text{-Sb}_3\text{-O-GO}$ surfaces. This is in consistent with the eCO₂RR performances test results, i.e., $\text{Sn}_7\text{-Sb}_3\text{-O-GO}$ exhibits an excellent HCOOH selectivity while $\text{SnO}_2\text{-GO}$ produces both HCOOH and

CO .

To obtain further information for the role of Sb on $\text{Sn}_x\text{-Sb}_y\text{-O-GO}$ NSs in eCO₂RR, the first-principles calculations based on density functional theory (DFT) calculations were performed on pure $\text{SnO}_2\text{-GO}$ and dual-active-site $\text{Sn}_7\text{-Sb}_3\text{-O-GO}$. The optimized structures of the reactants, intermediates (OCHO^* , HCOOH^* , $^{*\text{COOH}}$, $^{*\text{CO}}$ and H^*) on Sn site of $\text{SnO}_2\text{-GO}$, Sn site of $\text{Sn}_7\text{-Sb}_3\text{-O-GO}$ and Sb site of $\text{Sn}_7\text{-Sb}_3\text{-O-GO}$ are shown in Fig. 4c and Fig. S12 ~ S14. The density of states (DOS) for $\text{SnO}_2\text{-GO}$ and $\text{Sn}_7\text{-Sb}_3\text{-O-GO}$ is presented in Fig. 4d & e, respectively. Compared to the $\text{SnO}_2\text{-GO}$, the incorporation of Sb site into SnO_2 can narrow the band gap of $\text{Sn}_7\text{-Sb}_3\text{-O-GO}$, increasing the electron transfer rate. According to the experimental results, the activation of CO_2 mainly occurs on the Sn site, where CO_2 acquires an electron/proton pair or adsorbed H^* intermediate leading to the formation of two main reaction paths: (i) bounding OCHO^* (the key intermediate for HCOOH) via two oxygen atoms, (ii) or bounding $^{*\text{COOH}}$ (the key intermediate for CO) via carbon atom. For the HCOOH pathway, the Sn site of $\text{Sn}_7\text{-Sb}_3\text{-O-GO}$ reveals the Gibbs free energy (ΔG) for the formation of OCHO^* and HCOOH^* are 0.12 and 0.21 eV , which are lower than that of Sn site of $\text{SnO}_2\text{-GO}$ (1.0 eV and 0.39 eV) and Sb site of $\text{Sn}_7\text{-Sb}_3\text{-O-GO}$ (0.8 and 0.59 eV) as illustrated in Fig. 4f. It is worth noting that after introduction

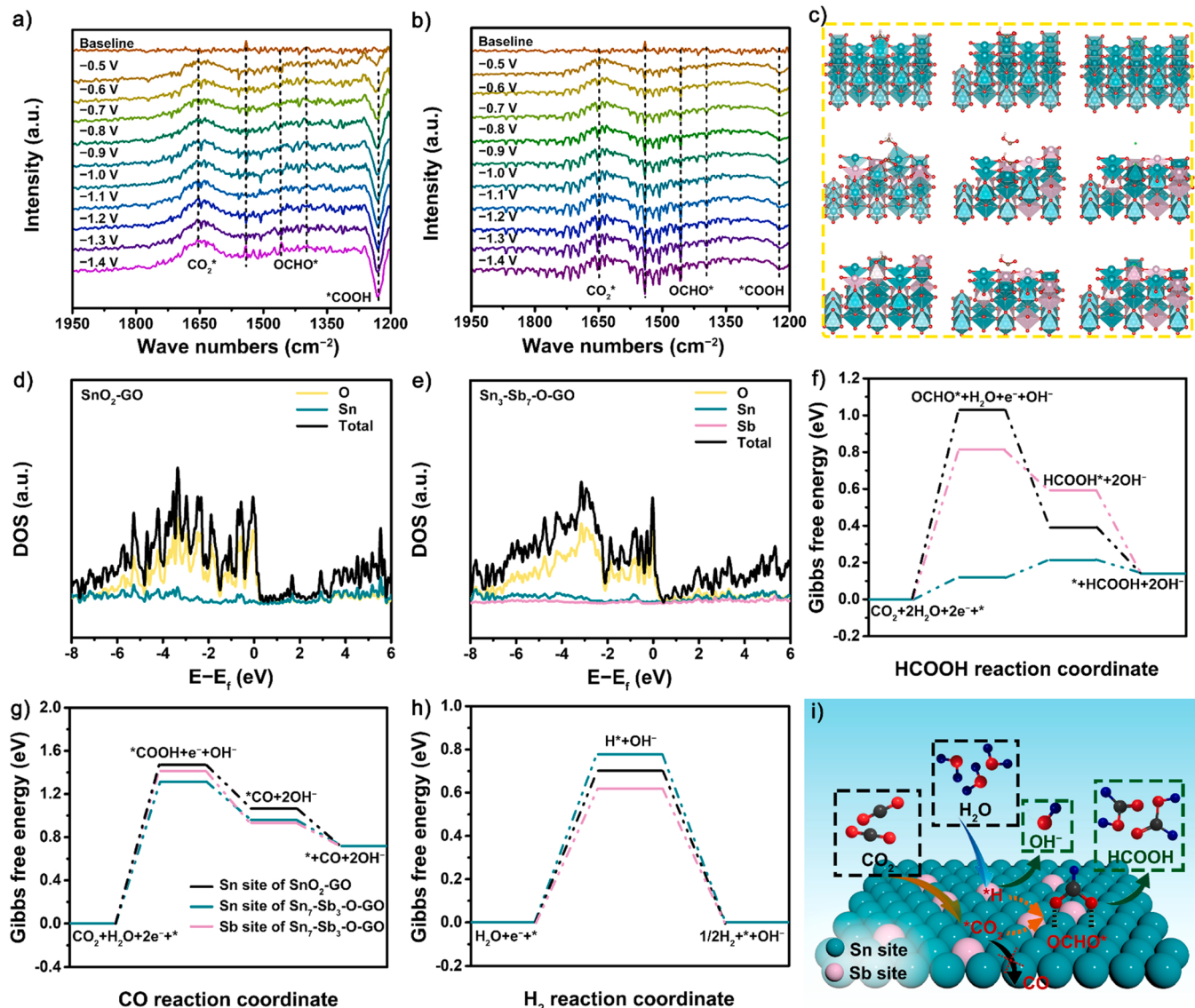


Fig. 4. In situ ATR-FTIR spectra of a) Sn₂-GO NSs and b) Sn₇-Sb₃-O-GO NSs. c) Calculated crystal structure of OCHO^{*}, *COOH and H^{*} on Sn site of Sn₂-GO, Sn site of Sn₇-Sb₃-O-GO and Sb site of Sn₇-Sb₃-O-GO, top to bottom successively. Calculated DOS of d) Sn₂-GO and e) Sn₇-Sb₃-O-GO. Gibbs free energies for f) HCOOH reaction coordinate, g) CO reaction coordinate and h) H₂ reaction coordinate on Sn site of Sn₂-GO, Sn site of Sn₇-Sb₃-O-GO and Sb site of Sn₇-Sb₃-O-GO. i) Schematic illustration for the reaction path.

of Sb site, the rate-limiting step turned out to be the formation of HCOOH^{*}, rather than OCHO^{*}, demonstrating that the HCOOH pathway is significantly favourable. For the CO pathway, the ΔG for the formation of *COOH and CO^{*} is also weakly descending on Sn site of Sn₇-Sb₃-O-GO (Fig. 4g), which are 1.31 and 0.96 eV (Sn site of Sn₂-GO are 1.46 and 1.06 eV, Sb site of Sn₇-Sb₃-O-GO are 1.41 and 0.93 eV). However, the energy-favourable HCOOH pathway have suppressed the competitive CO formation, resulting in the superior selectivity for HCOOH production in eCO₂RR performances test. Furthermore, we have further calculated the ΔG for the HER (Fig. 4h), where the lower formation energy of H^{*} species on Sb site (0.60 eV) in Sn₇-Sb₃-O-GO in comparison to the Sn site of Sn₇-Sb₃-O-GO (0.78 eV) and Sn₂-GO (0.71 eV), indicating that there is a higher activity of H₂O dissociation on Sb site which is beneficial to form the adsorbed H^{*} intermediate. It has been reported that the adsorbed H^{*} intermediate can boot the activation of CO₂ on adjacent Sn site to form the key intermediate of OCHO^{*}, thereby enabling electrochemical CO₂ reduction to HCOOH (Fig. 4i).

4. Conclusion

In summary, we present a Sn-Sb dual-active sites strategy for the first time, and construct a family of large-size ultrathin dual-active sites Sn_x-Sb_y-O-GO NSs, where higher electronegativity of Sb leads to the electron to easily flow from Sn to Sb and strengthening the interaction with the OCHO^{*} intermediate. Meanwhile, the large-size ultrathin nanosheet structure possesses ultrahigh surface-to-volume ratio and controllable Sn/Sb ratio, can tune eCO₂RR to HCOOH and suppress the CO process. The optimized Sn₇-Sb₃-O-GO catalyst exhibits an excellent HCOOH FE of 96.5% and a partial current density of -21.6 mA cm^{-2} at the potential of -1.1 V in 0.5 M KHCO₃ solution, as well as long durability over 21 h. The experiments and theory calculations demonstrate that the Sb secondary site can assist water activation for forming unique H^{*} species, and promote the binding strength of OCHO^{*} key intermediates on Sn_x-Sb_y-O-GO surfaces, thereby enhancing the HCOOH selectivity in eCO₂RR. This work lends credence to the design strategy of bimetallic dual-active sites for eCO₂RR sustainable energy conversion.

CRediT authorship contribution statement

Haichuan He: Conceptualization, Methodology, Investigation, Formal analysis, Visualization, Writing – original draft, Writing – review & editing. **Jian Wu:** Conceptualization, Validation, Formal analysis. **Xiao Yu:** Investigation, Visualization. **Dan Xiao:** Data curation, Software. **Yan Wang:** Data curation, Formal analysis. **Fei Chen:** Data curation, Investigation. **Dr. Liqiang Wang:** Data curation, Investigation. **Dr. Linlin Wu:** Conceptualization. **Dr. Jianhan Huang:** Conceptualization, Methodology, Visualization. **Dr. Ning Zhao:** Methodology, Visualization. **Dr. Liu Deng:** Conceptualization, Methodology, Visualization, Writing – original draft, Writing – review & editing. **Dr. You-Nian Liu:** Corresponding author, Supervision, Conceptualization, Writing – original draft, Writing – review & editing.

Declaration of Competing Interest

The authors declare that they have no known competing financial interests or personal relationships that could have appeared to influence the work reported in this paper.

Acknowledgements

This work was supported by the National Natural Science Foundation of China (Nos. 21636010, 21878342 and 22178393), the Foundation of State Key Laboratory of Coal Conversion, Shanxi, China (Grant No. J21-22-609), and the Hunan Provincial Science and Technology Plan Project, China (No. 2019TP1001 and 2020JJ3044).

Appendix A. Supporting information

Supplementary data associated with this article can be found in the online version at [doi:10.1016/j.apcatb.2022.121171](https://doi.org/10.1016/j.apcatb.2022.121171).

References

- [1] S. Abner, A. Chen, Design and mechanistic study of advanced cobalt-based nanostructured catalysts for electrochemical carbon dioxide reduction, *Appl. Catal. B Environ.* 301 (2021), 120761, <https://doi.org/10.1016/j.apcatb.2021.120761>.
- [2] L. Wang, P. Liu, Y. Xu, Y. Zhao, N. Xue, X. Guo, L. Peng, Y. Zhu, M. Ding, Q. Wang, W. Ding, Enhanced catalytic activity and stability of bismuth nanosheets decorated by 3-aminopropyltriethoxysilane for efficient electrochemical reduction of CO₂, *Appl. Catal. B Environ.* 298 (2021), 120602, <https://doi.org/10.1016/j.apcatb.2021.120602>.
- [3] H. He, K. Liu, K. Liang, A. Mustapha, Z. Wang, L. Wu, C. Yang, L. Deng, S. Guo, Y.-N. Liu, Boosting carbon dioxide electroreduction to C1 feedstocks via theory-guided tailoring oxygen defects in porous tin-oxide nanocubes, *J. Catal.* 385 (2020) 246–254, <https://doi.org/10.1016/j.jcat.2020.03.015>.
- [4] D.H. Nam, P. De Luna, A. Rosas-Hernandez, A. Thevenon, F. Li, T. Agapie, J. C. Peters, O. Shekhah, M. Eddaoudi, E.H. Sargent, Molecular enhancement of heterogeneous CO₂ reduction, *Nat. Mater.* 19 (2020) 266–276, <https://doi.org/10.1038/s41563-020-0610-2>.
- [5] H. He, C. Yang, L. Deng, J. Wu, F. Chen, J. Huang, Y.-N. Liu, Inside-mode indium oxide/carbon nanotubes for efficient carbon dioxide electroreduction by suppressing hydrogen evolution, *Chem. Commun.* 57 (2021) 1234–1237, <https://doi.org/10.1039/d0cc07417a>.
- [6] Z. Geng, Y. Cao, W. Chen, X. Kong, Y. Liu, T. Yao, Y. Lin, Regulating the coordination environment of Co single atoms for achieving efficient electrocatalytic activity in CO₂ reduction, *Appl. Catal. B Environ.* 240 (2019) 234–240, <https://doi.org/10.1016/j.apcatb.2018.08.075>.
- [7] B. Zhang, J. Zhang, P. An, Z. Su, Q. Wan, X. Tan, L. Zheng, Steering CO₂ electroreduction toward methane or ethylene production, *Nano Energy* 88 (2021), 106239, <https://doi.org/10.1016/j.nanoen.2021.106239>.
- [8] T. Zhang, X. Li, Y. Qiu, P. Su, W. Xu, H. Zhong, H. Zhang, Multilayered Zn nanosheets as an electrocatalyst for efficient electrochemical reduction of CO₂, *J. Catal.* 357 (2018) 154–162, <https://doi.org/10.1016/j.jcat.2017.11.003>.
- [9] L. Lv, X. He, J. Wang, Y. Ruan, S. Ouyang, H. Yuan, T. Zhang, Charge localization to optimize reactant adsorption on KCu_xS₄/CuO interfacial structure toward selective CO₂ electroreduction, *Appl. Catal. B Environ.* 298 (2021), 120531, <https://doi.org/10.1016/j.apcatb.2021.120531>.
- [10] H. Rabiee, L. Ge, X. Zhang, S. Hu, M. Li, S. Smart, Z. Zhu, H. Wang, Z. Yuan, Stand-alone asymmetric hollow fiber gas-diffusion electrodes with distinguished bronze phases for high-efficiency CO₂ electrochemical reduction, *Appl. Catal. B Environ.* 298 (2021), 120538, <https://doi.org/10.1016/j.apcatb.2021.120538>.
- [11] Y. Chen, B. Gao, M. Wang, X. Xiao, A. Lv, S. Jiao, P.K. Chu, Dual-phase MoC-Mo₂C nanosheets prepared by molten salt electrochemical conversion of CO₂ as excellent electrocatalysts for the hydrogen evolution reaction, *Nano Energy* 90 (2021), 106533, <https://doi.org/10.1016/j.nanoen.2021.106533>.
- [12] R.G. Mariano, M. Kang, O.J. Wahab, I.J. McPherson, J.A. Rabinowitz, P.R. Unwin, M.W. Kanan, Microstructural origin of locally enhanced CO₂ electroreduction activity on gold, *Nat. Mater.* 20 (2021) 1000–1006, <https://doi.org/10.1038/s41563-021-00958-9>.
- [13] B.S. Natinsky, C. Liu, Two are better than one, *Nat. Chem.* 11 (2019) 200–201, <https://doi.org/10.1038/s41557-019-0221-1>.
- [14] D.A. Salvatore, C.M. Gabardo, A. Reyes, C.P. O'Brien, S. Holdcroft, P. Pintauro, B. Bahar, M. Hickner, C. Bae, D. Sinton, E.H. Sargent, C.P. Berlinguet, Designing anion exchange membranes for CO₂ electrolyzers, *Nat. Energy* 6 (2021) 339–348, <https://doi.org/10.1038/s41560-020-00761-x>.
- [15] Z. Yang, H. Wang, X. Fei, W. Wang, Y. Zhao, X. Wang, X. Tan, Q. Zhao, H. Wang, J. Zhu, L. Zhou, H. Ning, M. Wu, MOF derived bimetallic CuBi catalysts with ultra-wide potential window for high-efficient electrochemical reduction of CO₂ to formate, *Appl. Catal. B Environ.* 298 (2021), 120571, <https://doi.org/10.1016/j.apcatb.2021.120571>.
- [16] J. Pei, T. Wang, R. Stui, X. Zhang, D. Zhou, F. Qin, X. Zhao, Q. Liu, W. Yan, J. Dong, L. Zheng, A. Li, J. Mao, W. Zhu, W. Chen, Z. Zhuang, N-Bridged Co-N-Ni: new bimetallic sites for promoting electrochemical CO₂ reduction, *Energy Environ. Sci.* 14 (2021) 3019–3028, <https://doi.org/10.1039/DEEE03947K>.
- [17] Z. Zhang, G. Wen, D. Luo, B. Ren, Y. Zhu, R. Gao, H. Dou, G. Sun, M. Feng, Z. Bai, A. Yu, Z. Chen, "Two ships in a bottle" design for Zn-Ag-O catalyst enabling selective and long-lasting CO₂ electroreduction, *J. Am. Chem. Soc.* 143 (2021) 6855–6864, <https://doi.org/10.1021/jacs.0c12418>.
- [18] L. Peng, Y. Wang, Y. Wang, N. Xu, W. Lou, P. Liu, D. Cai, H. Huang, J. Qiao, Separated growth of Bi-Cu bimetallic electrocatalysts on defective copper foam for highly converting CO₂ to formate with alkaline anion-exchange membrane beyond KHCO₃ electrolyte, *Appl. Catal. B Environ.* 288 (2021), 120003, <https://doi.org/10.1016/j.apcatb.2021.120003>.
- [19] X.F. Qiu, H.L. Zhu, J.R. Huang, P.Q. Liao, X.M. Chen, Highly selective CO₂ electroreduction to C₂H₄ using a metal-organic framework with dual active sites, *J. Am. Chem. Soc.* 143 (2021) 7242–7246, <https://doi.org/10.1021/jacs.1c01466>.
- [20] W. Ma, S. Xie, X.G. Zhang, F. Sun, J. Kang, Z. Jiang, Q. Zhang, D.Y. Wu, Y. Wang, Promoting electrocatalytic CO₂ reduction to formate via sulfur-boosting water activation on indium surfaces, *Nat. Commun.* 10 (2019) 892, <https://doi.org/10.1038/s41467-019-08805-x>.
- [21] F. Li, Y.C. Li, Z. Wang, J. Li, D.-H. Nam, Y. Lum, M. Luo, X. Wang, A. Ozden, S.-F. Hung, B. Chen, Y. Wang, J. Wicks, Y. Xu, Y. Li, C.M. Gabardo, C.-T. Dinh, Y. Wang, T.-T. Zhuang, D. Sinton, E.H. Sargent, Cooperative CO₂-to-ethanol conversion via enriched intermediates at molecule–metal catalyst interfaces, *Nat. Catal.* 3 (2019) 75–82, <https://doi.org/10.1038/s41929-019-0383-7>.
- [22] X. Wang, A. Xu, F. Li, S.F. Hung, D.H. Nam, C.M. Gabardo, Z. Wang, Y. Xu, A. Ozden, A.S. Rasouli, A.H. Ip, D. Sinton, E.H. Sargent, Efficient Methane Electrosynthesis Enabled by Tuning Local CO₂ Availability, *J. Am. Chem. Soc.* 142 (2020) 3525–3531, <https://doi.org/10.1021/jacs.9b12445>.
- [23] X. Zhi, Y. Jiao, Y. Zheng, A. Vasileff, S.-Z. Qiao, Selectivity roadmap for electrochemical CO₂ reduction on copper-based alloy catalysts, *Nano Energy* 71 (2020), 104601, <https://doi.org/10.1016/j.nanoen.2020.104601>.
- [24] S. Rasul, A. Pugnat, H. Xiang, J.-M. Fontmorin, E.H. Yu, Low cost and efficient alloy electrocatalysts for CO₂ reduction to formate, *J. CO₂ Util.* 32 (2019) 1–10, <https://doi.org/10.1016/j.jcou.2019.03.016>.
- [25] S. Ning, J. Wang, D. Xiang, S. Huang, W. Chen, S. Chen, X. Kang, Electrochemical reduction of SnO₂ to Sn from the Bottom: In-Situ formation of SnO₂/Sn heterostructure for highly efficient electrochemical reduction of carbon dioxide to formate, *J. Catal.* 399 (2021) 67–74, <https://doi.org/10.1016/j.jcat.2021.04.028>.
- [26] W. Ren, X. Tan, J. Qu, S. Li, J. Li, X. Liu, S.P. Ringer, J.M. Cairney, K. Wang, S. C. Smith, C. Zhao, Isolated copper-tin atomic interfaces tuning electrocatalytic CO₂ conversion, *Nat. Commun.* 12 (2021) 1449, <https://doi.org/10.1038/s41467-021-21750-y>.
- [27] Z. Chen, T.T. Fan, Y.Q. Zhang, J. Xiao, M.R. Gao, N.Q. Duan, J.W. Zhang, J.H. Li, Q. X. Liu, X.D. Yi, J.L. Luo, Wavy SnO₂ catalyzed simultaneous reinforcement of carbon dioxide adsorption and activation towards electrochemical conversion of CO₂ to HCOOH, *Appl. Catal. B Environ.* 261 (2020), 118243, <https://doi.org/10.1016/j.apcatb.2019.118243>.
- [28] Y. Pi, J. Guo, Q. Shao, X. Huang, All-inorganic SrSnO₃ perovskite nanowires for efficient CO₂ electroreduction, *Nano Energy* 62 (2019) 861–868, <https://doi.org/10.1016/j.nanoen.2019.05.077>.
- [29] D. Li, J. Wu, T. Liu, J. Liu, Z. Yan, L. Zhen, Y. Feng, Tuning the pore structure of porous tin foam electrodes for enhanced electrochemical reduction of carbon dioxide to formate, *Chem. Eng. J.* 375 (2019), 122024, <https://doi.org/10.1016/j.cej.2019.122024>.
- [30] Q. Yang, Q. Wu, Y. Liu, S. Luo, X. Wu, X. Zhao, H. Zou, B. Long, W. Chen, Y. Liao, L. Li, P.K. Shen, L. Duan, Z. Quan, Novel Bi-doped amorphous SnO_x nanoshells for efficient electrochemical CO₂ reduction into formate at low overpotentials, *Adv. Mater.* 32 (2020), e2002822, <https://doi.org/10.1002/adma.202002822>.
- [31] A. Zhang, R. He, H. Li, Y. Chen, T. Kong, K. Li, H. Ju, J. Zhu, W. Zhu, J. Zeng, Nickel Doping in Atomically Thin Tin Disulfide Nanosheets Enables Highly Efficient CO₂ Reduction, *Angew. Chem. Int. Ed.* 57 (2018) 10954–10958, <https://doi.org/10.1002/anie.201806043>.
- [32] P. Han, Z. Wang, M. Kuang, Y. Wang, J. Liu, L. Hu, L. Qian, G. Zheng, 2D assembly of confined space toward enhanced CO₂ electroreduction, *Adv. Energy Mater.* 8 (2018) 801230–803274, <https://doi.org/10.1002/aenm.201801230>.

- [33] L. Zhang, X.X. Li, Z.L. Lang, Y. Liu, J. Liu, L. Yuan, W.Y. Lu, Y.S. Xia, L.Z. Dong, D. Q. Yuan, Y.Q. Lan, Enhanced Cuprophilic Interactions in Crystalline Catalysts Facilitate the Highly Selective Electroreduction of CO₂ to CH₄, *J. Am. Chem. Soc.* 143 (2021) 3808–3816, <https://doi.org/10.1021/jacs.0c11450>.
- [34] Y. Song, J.R.C. Junqueira, N. Sikdar, D. Ohl, S. Dieckhofer, T. Quast, S. Seisel, J. Masa, C. Andronescu, W. Schuhmann, B-Cu-Zn gas diffusion electrodes for CO₂ electroreduction to C₂₊ products at high current densities, *Angew. Chem. Int. Ed.* 60 (2021) 9135–9141, <https://doi.org/10.1002/anie.202016898>.
- [35] H. Liu, J. Xia, N. Zhang, H. Cheng, W. Bi, X. Zu, W. Chu, H. Wu, C. Wu, Y. Xie, Solid–liquid phase transition induced electrocatalytic switching from hydrogen evolution to highly selective CO₂ reduction, *Nat. Catal.* 4 (2021) 202–211, <https://doi.org/10.1038/s41929-021-00576-3>.
- [36] Y.-W. Choi, F. Scholten, I. Sinev, B.R. Cuenya, Enhanced stability and CO/formate selectivity of plasma-treated SnO_x/AgO_x catalysts during CO₂ electroreduction, *J. Am. Chem. Soc.* 141 (2019) 5261–5266, <https://doi.org/10.1021/jacs.8b12766>.
- [37] X. Zheng, Y. Ji, J. Tang, J. Wang, B. Liu, H.-G. Steinrück, K. Lim, Y. Li, M.F. Toney, K. Chan, Y. Cui, Theory-guided Sn/Cu alloying for efficient CO₂ electroreduction at low overpotentials, *Nat. Catal.* 2 (2018) 55–61, <https://doi.org/10.1038/s41929-018-0200-8>.
- [38] W. Zhang, Q. Qin, L. Dai, R. Qin, X. Zhao, X. Chen, D. Ou, T.T. Chuong, B. Wu, N. Zheng, Electrochemical reduction of CO₂ to CH₃OH on hierarchical Pd/SnO₂ nanosheets with abundant Pd-O-Sn interfaces, *Angew. Chem. Int. Ed.* 57 (2018) 9475–9479, <https://doi.org/10.1002/anie.201804142>.
- [39] J. Wang, S. Ning, M. Luo, D. Xiang, W. Chen, X. Kang, Z. Jiang, S. Chen, In-Sn alloy core-shell nanoparticles: In-doped SnO_x shell enables high stability and activity towards selective formate production from electrochemical reduction of CO₂, *Appl. Catal. B Environ.* 288 (2021), 119979, <https://doi.org/10.1016/j.apcatb.2021.119979>.
- [40] D. Li, L. Huang, Y. Tian, T. Liu, L. Zhen, Y. Feng, Facile synthesis of porous Cu-Sn alloy electrode with prior selectivity of formate in a wide potential range for CO₂ electrochemical reduction, *Appl. Catal. B Environ.* 292 (2021), 120119, <https://doi.org/10.1016/j.apcatb.2021.120119>.
- [41] J. Wang, Y. Ji, Q. Shao, R. Yin, J. Guo, Y. Li, X. Huang, Phase and structure modulating of bimetallic CuSn nanowires boosts electrocatalytic conversion of CO₂, *Nano Energy* 59 (2019) 138–145, <https://doi.org/10.1016/j.nanoen.2019.02.037>.
- [42] B. Jiang, Y. Guo, J. Kim, A.E. Whitten, K. Wood, K. Kani, A.E. Rowan, J. Henzie, Y. Yamauchi, Mesoporous metallic iridium nanosheets, *J. Am. Chem. Soc.* 140 (2018) 12434–12441, <https://doi.org/10.1021/jacs.8b05206>.
- [43] L. Wang, K. Liang, L. Deng, Y.-N. Liu, Protein hydrogel networks: A unique approach to heteroatom self-doped hierarchically porous carbon structures as an efficient ORR electrocatalyst in both basic and acidic conditions, *Appl. Catal. B Environ.* 246 (2019) 89–99, <https://doi.org/10.1016/j.apcatb.2019.01.050>.
- [44] X. Wang, X. Li, S. Ding, Y. Chen, Y. Liu, M. Fang, G. Xiao, Y. Zhu, Constructing ample active sites in nitrogen-doped carbon materials for efficient electrocatalytic carbon dioxide reduction, *Nano Energy* 90 (2021), 106541, <https://doi.org/10.1016/j.nanoen.2021.106541>.
- [45] B. Zhang, M. Chen, C. Zhang, H. He, Electrochemical oxidation of gaseous benzene on a Sb-SnO₂/foam Ti nano-coating electrode in all-solid cell, *Chemosphere* 217 (2019) 780–789, <https://doi.org/10.1016/j.chemosphere.2018.10.222>.
- [46] R. Zhang, K. Li, S. Ren, J. Chen, X. Feng, Y. Jiang, Z. He, L. Dai, L. Wang, Sb-doped SnO₂ nanoparticle-modified carbon paper as a superior electrode for a vanadium redox flow battery, *Appl. Surf. Sci.* 526 (2020), 146685, <https://doi.org/10.1016/j.apsusc.2020.146685>.
- [47] H. Zhao, Y. Zhu, F. Li, R. Hao, S. Wang, L. Guo, A generalized strategy for the synthesis of large-size ultrathin two-dimensional metal oxide nanosheets, *Angew. Chem. Int. Ed.* 56 (2017) 8766–8770, <https://doi.org/10.1002/anie.201703871>.
- [48] Z. Teng, Q. Zhang, H. Yang, K. Kato, W. Yang, Y.-R. Lu, S. Liu, C. Wang, A. Yamakata, C. Su, B. Liu, T. Ohno, Atomically dispersed antimony on carbon nitride for the artificial photosynthesis of hydrogen peroxide, *Nat. Catal.* 4 (2021) 374–384, <https://doi.org/10.1038/s41929-021-00605-1>.
- [49] J. Staszak-Jirkovsky, C.D. Malliakas, P.P. Lopes, N. Danilovic, S.S. Kota, K. C. Chang, B. Genorio, D. Strmcnik, V.R. Stamenkovic, M.G. Kanatzidis, N. M. Markovic, Design of active and stable Co-Mo-Sx chalcogels as pH-universal catalysts for the hydrogen evolution reaction, *Nat. Mater.* 15 (2016) 197–203, <https://doi.org/10.1038/nmat4481>.
- [50] J. Sheng, Y. He, J. Li, C. Yuan, H. Huang, S. Wang, Y. Sun, Z. Wang, F. Dong, Identification of halogen-associated active sites on Bismuth-based perovskite quantum dots for efficient and selective CO₂-to-CO photoreduction, *ACS Nano* 14 (2020) 13103–13114, <https://doi.org/10.1021/acsnano.0c04659>.